Applied Catalysis B: Environmental 181 (2016) 413–419

Contents lists available at ScienceDirect

Applied Catalysis B: Environmental

journal homepage: www.elsevier.com/locate/apcatb

Condensed and low-defected graphitic carbon nitride with enhanced photocatalytic hydrogen evolution under visible light irradiation

Yanjuan Cui [a,*], Guigang Zhang [b], Zhenzhen Lin [b], Xinchen Wang [b]

[a] School of Environmental and Chemical Engineering, Jiangsu University of Science and Technology, Zhenjiang 212003, PR China
[b] State Key Laboratory of Photocatalysis on Energy and Environment, College of Chemistry, Fuzhou University, Fuzhou 350002, China

ARTICLE INFO

Article history:
Received 11 May 2015
Received in revised form 2 August 2015
Accepted 9 August 2015
Available online 12 August 2015

Keywords:
Carbon nitride
Ammonia
Thermal-polymerization
H_2 evolution

ABSTRACT

Condensed and low-defected graphitic carbon nitride (denoted as CNa) was synthesized from a simple one-step thermal polymerization in ammonia. The promotion effect in the structural evolution during condensation in ammonia and catalytic performance for H_2 evolution for the defected-C_3N_4 was well studied. Comparing to pristine g-C_3N_4 prepared from polymerization in nitrogen (CNn), the as-prepared sample has the same composition and graphitic stacking structure, but appears well dispersed flake morphology with larger surface area and more mesoporous texture. Surprisingly, this sample possessed much condensed crystallinity and improved in-plane conjugated network with decreased sp^2 N defects in heptazine heterocycle. Consequently, higher rate of photocatalytic H_2 production under visible light irradiation, about 6 times of CNn, was achieved, owing to the broader distribution of active sites and more efficient transport and separation of photogenerated charge carriers in the improved ordered skeleton microstructure.

1. Introduction

Semiconductor photo-driven water splitting is an attractive technological solution to convert solar energy in the form of chemical energy for the sunlight as a primary source of power [1–3]. Hydrogen has been regarded as a promising carbon-neutral alternative and an ideal clean fuel carrier. Since the discovery of hydrogen generation from water by TiO_2-based photoelectrochemical cells in 1972, enormous efforts have been made to establish a stable photocatalytic water splitting system. So far, inorganic semiconductors are typically used as solid photocatalysts for H_2 evolution, including metal (oxy) nitrides, (oxy) sulfides, etc. [4,5]. However, most of them contain expensive and/or precious metal components, still far from meeting industrial requirements of economy and stability.

Recently, notable advances in heterogeneous photocatalysis have been made using metal-free graphitic carbon nitrides (g-C_3N_4) as light antennae to mediate electron and energy transfers for artificial photosynthesis [6–9]. With suitable electronic structure (conduction band at −1.3 V and valance band at 1.4 V vs NHE, pH = 7), it could work as a stable photocatalyst for H_2 production from water under visible light. However, due to the high exciton binding energy of polymer, C_3N_4 shows just moderate activity and low quantum efficiency during the water splitting process. To improve its photocatalytic efficiency, great efforts have been made on modification of C_3N_4, including chemical structure adjustment and nanostructure design, such as fabricating pore structure [10,11], doping with heteroatoms (C, B, S) [12–14], coupling with other semiconductors [15,16], controlling morphology [17,18], and copolymerizing with organic molecules [19,20], etc. As a result of these strategies, the photocatalytic activity for H_2 evolution of C_3N_4 has been much improved.

It is clear from theoretical studies that the optoelectronic properties of C_3N_4 can be affected by the degree of polymer condensation. This result leads to C_3N_4 with tunable optoelectronic properties depending on the synthesis and processing conditions. Up to now, large amount of defects exists in g-C_3N_4 nanostructure derived from incomplete polymerization during high temperature sintering process [21,22]. These intrinsic defects are important, since its regulating effect of electronic structure in polymer [23,24]. On the other hand, charge carriers transport is linked to lattice disorder in the polymer, and more improved in the ordered regions of a heterogeneous microstructure [25]. The improvement of the crystallinity of g-C_3N_4, in principle, could promote the kinetics of charge diffusion in both the bulk and the surface as a result of fewer defects in the network. So many modification methods aforementioned

* Corresponding author. Fax: +86 511 85605157.
E-mail address: yjcui@just.edu.cn (Y. Cui).

http://dx.doi.org/10.1016/j.apcatb.2015.08.018
0926-3373/

towards g-C_3N_4, although indeed improved its structure and photocatalytic performance to some extent, also increased the defects numbers, caused structure disorder and lower crystallinity [22,26].

As an alternative approach, promoting polymerization degree of g-C_3N_4 has been shown to increase the photocatalytic activity. For example, cross-linked CN/rGO, NiS/C_3N_4, and C-PDA-g-C_3N_4 composites with improved stacking structure were obtained, probably due to the increase in structural correlation introduced by nanosheets or inching control of the polymerization process [27–29]. These strategies for strengthening the condense structure for C_3N_4-based material mainly make use of strong interaction force generated between 2D materials and the impact factors for improved photocatalytic activity mainly from the building of heterostructure, rather than condensed structure. In allusion to improve the crystallinity of intrinsic C_3N_4, controlling thermal-polymerization temperature was a simple approach, but had little effect [30]. In addition, Li et al. prepared C_3N_4 nanorods with a more condensed network using AAO membrane as a template [31]. Alkaline hydrothermal treatment of C_3N_4 was undertaken to remove unstable domains of not-well-ordered C_3N_4 by hydrolysis [32]. From these process optimizations, the defects level of C_3N_4 was decreased and the degree of polymerization was improved. However, the optimization merely confined to the surface structure and interlayer arrangement. Therefore, currently, persistent efforts are still needed to improve the microstructure of g-C_3N_4.

In this paper, low defected-C_3N_4 (CNa) with well condensed crystallinity has been prepared through a simple one-step ammonia thermal-polymerization process. The detailed structure and property of the resultant novel C_3N_4 material was examined. It was found that the microstructure of heptazine conjugated system could be much optimized with more ordered network. As a result, the highly condensed CNa show a larger surface area and improved transport of photogenerated carriers, presumably due to strongly ordered π-stacks. As expected, CNa exhibit enhanced photocatalytic H_2 evolution under visible light irradiation.

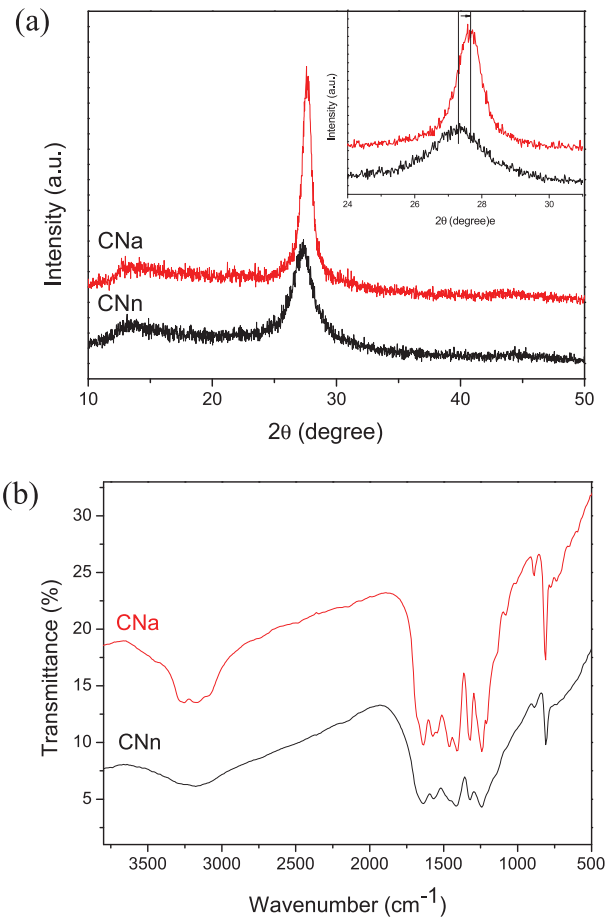

Fig. 1. Powder XRD patterns (a) and FT-IR spectra (b) of CNa and CNn.

2. Experimental

2.1. Preparation of catalysts

All the chemicals were reagent grade and used without further purification. Low-defected catalyst CNa was prepared via ammonia-polymerization approach. Certain amount of precursor ammonium thiocyanate (NH_4SCN) was calcined at 550 °C for 2 h with a ramp rate of 5 °C/min in ammonia atmosphere. Pristine catalyst CNn was prepared under the same conditions but in nitrogen atmosphere [33]. The agglomerates were milled into powder in an agate mortar for further characterization and performance measurements.

2.2. Catalyst characterization

X-ray diffraction (XRD) patterns of the samples were performed by using a Bruker D8 Advance X-ray diffractometer (Cu–Ka1 irradiation, λ = 1.5406 Å). Fourier transformed infrared (FTIR) spectra were recorded on a Nicolet Magna 670 FTIR spectrometer and the samples were mixed with KBr at a concentration of ca. 1 wt%. A Varian Cary 500 Scan UV–vis spectrophotometer was used to record the UV–vis diffuse reflectance spectra of samples with $BaSO_4$ as the reference. Nitrogen adsorption–desorption isotherms were collected at a Micromeritics ASAP 2020 surface area and porosity analyzer. X-ray photoelectron spectroscopy (XPS) measurements were performed on a Thermo Scientific ESCA Lab 250 spectrometer which consists of a monochromatic Al Kα as the X-ray source. All the binding energies were calibrated by the C 1s peak of the surface adventitious carbon at 284.6 eV. The thermal stability of the as-prepared samples was verified using a thermogravimetric analyzer (PerkinElmer TGA7). The morphology of the samples was investigated by field emission scanning electron microscopy (SEM) (JSM-6700F). Transmission electron microscopy (TEM) was carried out using a JEOL model JEM 2010 EX instrument. Steady fluorescence emission spectra were recorded at room temperature under excitation at 420 nm with a fluorescence spectrophotometer (Edinburgh Instruments, FLSP-920).

2.3. Measurement of photocatalytic activity

The photocatalytic reactions were carried out in a Pyrex top-irradiation reaction vessel connected to a closed gas circulation and evacuation system. H_2 production was performed by dispersing 50 mg of catalyst powder in an aqueous solution (100 mL) containing triethanolamine (10 vol%) as a sacrificial electron donor. 100 μL of H_2PtCl_6 aqueous solution (Sigma–Aldrich, 0.015 g mL^{-1} based on Pt) was added to the reaction solution for Pt in situ photodeposition on the surface of the catalyst. The reactant solution was degassed several times to remove air prior to irradiation under a 300 W Xenon lamp equipped with 420 nm optical cut-off filters. The temperature of the reaction solution was maintained at room temperature by the flow of cooling water during the reaction. The amount of H_2 production was analyzed using an online gas chromatography.

3. Results and discussions

Fig. 1a presents the XRD patterns of as-prepare CNa catalyst and CNn as pristine g-C_3N_4 for a reference. It can be seen that both materials show a highly resembled typical g-C_3N_4 layered structure at ~27.3° and ~13.0° without an impurity phase. These two distinct diffraction peaks belong to the long-range interplanar stacking of aromatic systems identified as the (0 0 2) peak and the in-plane structural packing motif as the (1 0 0) peak, respectively [34]. Impressively, the intensity of the main (0 0 2) peak is much increased and becomes narrower, indicating much higher long-range order of the interplanar structure packing in the g-C_3N_4 sheets. In addition, the (0 0 2) peak displays a slight shift to higher angles from 27.3° to 27.6°, corresponding to a reduction in the stacking distance from 0.326 to 0.322 nm of graphitic layered structure [35]. According to Bragg's law, this up-shift indicates the slightly more dense packing of the conjugated systems than the pristine g-C_3N_4 produced by the ammonia polymerization [36]. That is to say, a significant structural improvement of the material is obtained since the increased degree of condensation. Whereas the intensity and position of the peak (1 0 0) remains unchanged, it suggests the stable maintained in-plane heptazine conjugated structure of CNa skeleton.

The spectra of both CNn and low-defected CNa show the typical IR patterns of graphitic carbon nitride (Fig. 1b) [37]. The strong bands at 1200–1600 cm^{-1} are assigned to the stretching vibration of either trigonal C—N(—C)—C or bridging C—NH—C units in the heptazine heterocyclic ring (C6N7) units, while the sharp peak at ~810 cm^{-1} is considered as their breathing mode. These peaks indicate the existence of the basic melon units with NH/NH_2 groups. The broad peak located at 2900–3300 cm^{-1} is attributed to the uncondensed amino groups and the absorbed H_2O molecules. We can see that the crystal structure of CNa is basically the same to that of CNn, but the peak intensity and stretching modes of the skeletal CNa network are enhanced and better resolved, probably due to the better organization of conjugated system which indicating the higher condensation of C_3N_4.

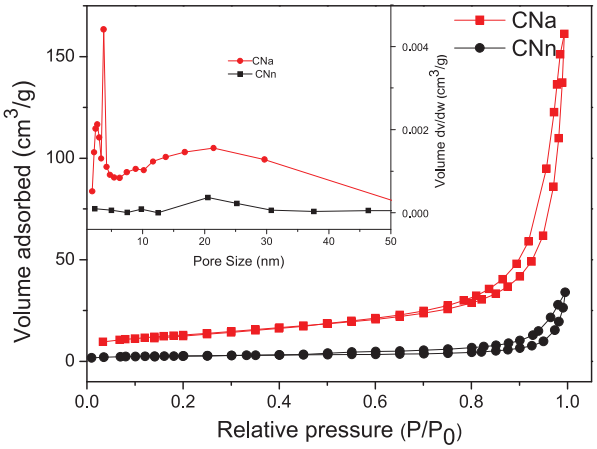

Fig. 2. N_2 adsorption–desorption isotherms for CNa and CNn. The insert is the corresponding BJH pore-size distribution curves.

The texture of the CNa and CNn samples were characterized by nitrogen adsorption–desorption measurements. The isotherms and the Barrett–Joyner–Halenda (BJH) pore size distributions are shown in Fig. 2. It can be seen that both samples possess Type IV adsorption–desorption isotherms with H3 hysteresis loop in the relative pressure range of 0.6–1.0, proving the existence of mesopores connected via micropores. The specific surface area and pore volume of the CNa is estimated about 46 m^2/g and 0.25 cm^3/g, which is about 5 times larger than that of pristine CNn (9 m^2/g, 0.05 cm^3/g). This could be ascribed to the structural optimization of CNa during the ammonia-polymerization process. Ammonia as alkaline gas could well interaction with the precursor molecule and promote the escape of acid gas. The bulk structure of C_3N_4 became loosen and turned to porosity. The large surface area and pore volume could provide more reactive sites, in order to adsorb more

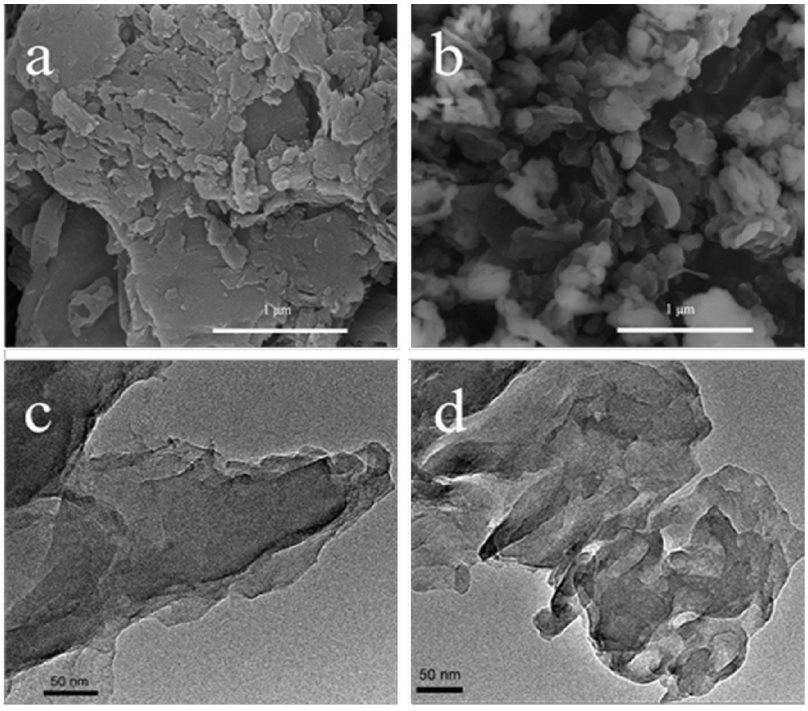

Fig. 3. SEM and TEM images of CNn (a,c) and CNa (b,d).

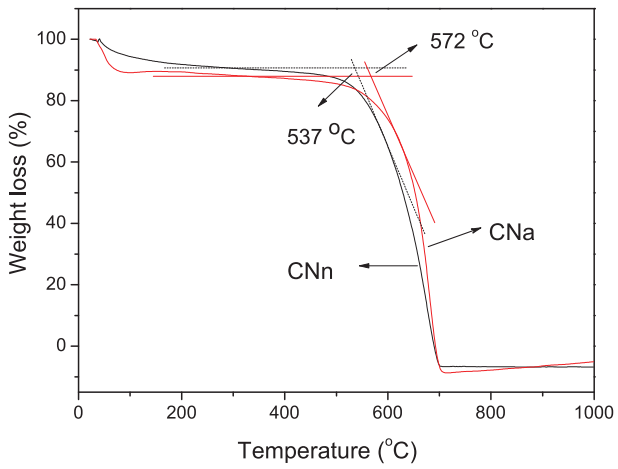

Fig. 4. Thermogravimetric analysis (TGA) for heating CNa and CNn under nitrogen.

reactants and conducive to mass transfer during photocatalytic process.

The local morphologies of synthesized materials were performed in SEM. Fig. 3a demonstrates that the CNn sample was composed of block large particles with a layer structure, which consistent with previous reports [37]. It is easy to find in Fig. 3b for CNa samples prepared in the ammonia conditions that it has smaller particle size and better dispersion with petaloid morphology. To obtain more information about the local morphologies of the samples, TEM analysis was carried out. As shown in Fig. 3d, compared to the pristine g-C_3N_4 consisting of typical bulk layered structure, image of CNa samples appears layered platelet-like surface morphology with many pores decorated on the sheet network. Furthermore, the basic sheet edge tends to bend, which may caused as a result of minimizing the surface energy of the sheet and porous structure formation. These characteristics bespeak much high surface area of samples obtained in ammonia and are in agreement with the results of the above nitrogen adsorption–desorption analysis.

Thermogravimetric analysis (TGA) was carried out in N_2 atmosphere (see Fig. 4) to evaluate the thermodynamic stability of as-prepared samples. Below 200 °C, ~15% weight loss occurs in CNa, which originated from the desorption of adsorbed H_2O or CO_2 on the surface of catalyst. The increased weight loss (~10% for CNn) reflects the significant surface expansion. When the temperature increased up to 570 °C, the CNa sample began to decompose rapidly. Compared to CNn, the decomposition temperature of CNa increase

Table 1
Physicochemical properties and photocatalytic activity of CNa and CNn for hydrogen evolution with visible light.

Catalysts	C/N (atomic)	BET[a] ($m^2\ g^{-1}$)	PV[b] ($cm^3\ g^{-1}$)	BG[c] (eV)	HER[d] ($\mu mol\ h^{-1}$)
CNn	0.76	9	0.05	2.62	55
CNa	0.75	46	0.25	2.87	303

[a] Surface area.
[b] Pore volume.
[c] Band gap.
[d] H_2 Evolution rate.

by about 35 °C, indicates improved thermal stability of CNa. Thus, higher thermodynamic stability for CNa further demonstrates the higher degree of polymerization.

The chemical states of CNa and CNn samples were investigated by the XPS technique, and the deconvoluted high-resolution C 1s and N 1s XPS spectra are shown in Fig. 5. Both of them present the C 1s core level spectrum with binding energies of 288.0 and 284.6 eV. The main contribution peak at 288.0 eV can be ascribed to sp2 hybridized carbon in the aromatic ring (C_{3N}). The C1s peak at 284.6 eV in the sample was typically assigned to graphitic carbon (C) or sp^2 C—N. The high-resolution N1s spectra also can be deconvoluted into two peaks, while the main component centered at 398.7 eV attributable to sp2 N involved in triazine rings (N_{2C}). This N=C linkage is viewed as the major building block of the heptazine-hybridized heterocycle. The contribution at 400.4 eV corresponded to bridging nitrogen atoms N—(C) 3 in heptazine unit (N_{3C}). These assignments of C1s and N1s agree well with the g-C_3N_4 reported previously [24]. The surface atomic ratio of carbon to nitrogen was 0.76 in the pristine CNn and 0.73 in the low-defected CNa. It confirmed that the element state and content of C_3N_4 was essentially almost unchanged under different synthetic atmosphere, even though the slight higher N content may root in more rich —NH2 group on the surface of CNa sample. After carefully analysis, we can observe that compared to CNn, apparent changes occur in C 1s and N 1s XPS spectra for CNa sample. The atomic ratio of C_{3N} to C and N_{2C} to N_{3C} decreases from 14.29 to 5.52 and 5.72 to 3.84, respectively (Tab. 2). These results clearly indicate that the heptazine unit of C_3N_4 in CNa tended to more complete and low-defects was exist in the sp2C—N conjugate framework.

Fig. 6 displays the UV–vis diffuse reflection spectra of as-prepared CNa and CNn samples. The spectra of C_3N_4 show intense absorption bands with steep edges, due to the visible-light induced transition of electrons from the valence band to the conduction band. The absorption band edge of CNn was at ca. 450 nm, corresponding to the band gap about 2.62 eV. Obviously, the optical band edges of CNa is maintained but indeed shifted to a shorter wave-

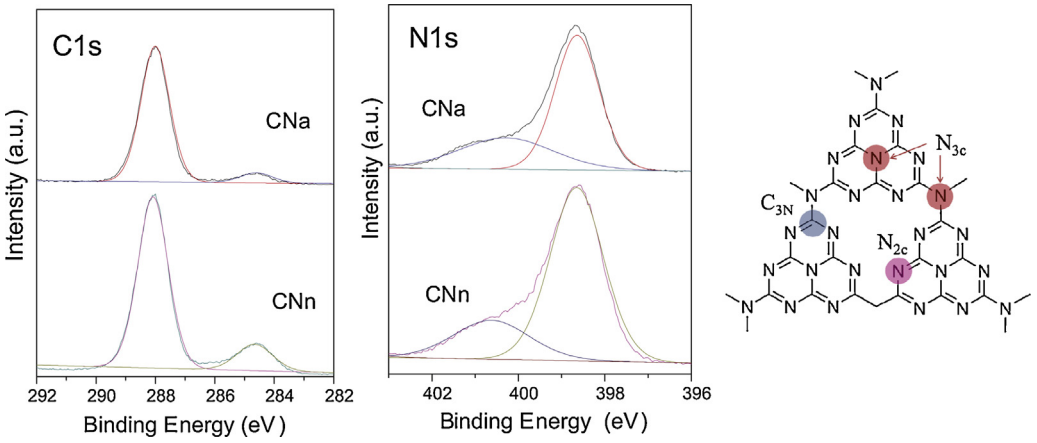

Fig. 5. Deconvoluted high-resolution C 1s and N 1s XPS spectra of CNa and CNn.

length and the band gap of it is broadened to 2.87 eV. The blue shifts can be explained by the well-known quantum confinement effect [38]. The remarkable increase in the bandgap by 0.25 eV improves the redox ability of charge carriers generated in the CN nanosheets. As might have been expected, CNa sample shows a less pronounced background level at the same position compares with CNn. This result further demonstrates a lower density of surface defect site [39].

The photoluminescence spectrum (PL) not only sensitively depends on the degree of condensation and the packing between the CN layers, but also reflects the separation and recombination of photogenerated charge carrier in semiconductors. As shown in Fig. 7, compared with CNn, the PL spectrum is blue shifted for CNa due to its tunable widening bandgap. The narrowing of its photoluminescence spectrum indicates the increase of the degree of its thermal condensation and the decrease amount of defect structures. This may be due to altered electronic coupling between the layers when going to a more perfected packing by condensation in ammonia for CNa [34,40,41].

Room-temperature EPR analysis was carried out to investigate the electronic band structure of as-prepared materials. In Fig. 8, one single Lorentzian line centered at a g value of 2.0034,which

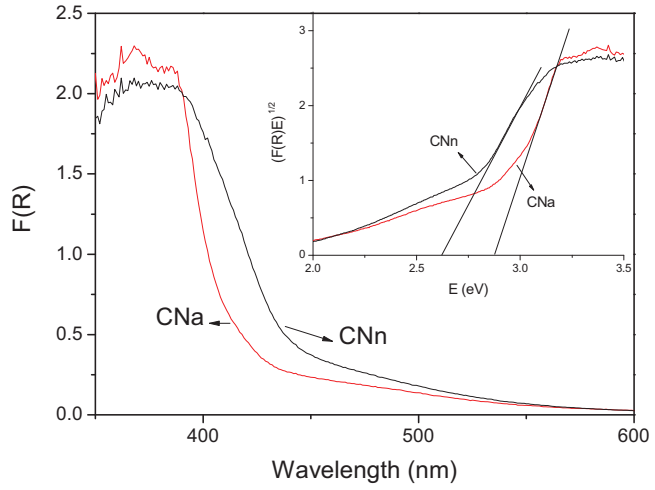

Fig. 6. UV–vis diffuse reflectance spectroscopy for CNa and CNn. The inset shows the bandgap determination form the Tauc plots.

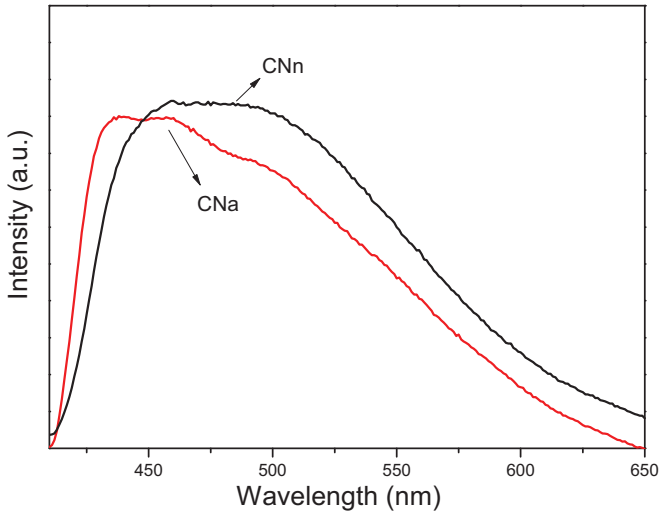

Fig. 7. Fluorescence emission spectra of CNa and CNn. The wavelength of excitation light for fluorescence emission spectra was 420 nm.

Table 2
Values of *N* and *C* species in the CNa and CNn.

	N (At%)		*C* (At%)	
	N_{2C}	N_{3C}	C_{3N}	*C*
CNa	45.20	7.97	37.44	2.62
CNn	42.01	10.93	34.01	6.16

is assigned to unpaired electrons in the aromatic rings of carbon atoms (conduction band electrons) in the localized π states of typical heptazine g-C_3N_4 [42], is observed for all of the samples in the magnetic field from 3465 to 3650 G, indicating the establishment of a semiconductor structure. No mater there is or no light irradiation, the EPR intensity of CNa is much higher than that of CNn sample, indicates the increased density state of conduction band in CNa catalyst. When irradiated by visible light, the EPR intensity of CNa catalyst further increase, certifying well photoelectric response. Excitedly, this ammonia-polymerization process improves the p-electron delocalization in the conjugated system of CNa with low-defection, thus the intrinsic optical and electronic properties of the resulting catalyst were greatly modified.

The photocatalytic activities of as-prepared C_3N_4 samples were evaluated by H_2 evolution reactions from aqueous proton solution, using 3 wt.% Pt as co-catalyst under visible light irradiation (λ > 420 nm). The Mott–Schottky plots measurement (Fig. S1) indicate that the conduction position of CNa was slightly cathodic shift (0.08 V), which thermodynamically enables photocatalytic water reduction. As expected, low-defected CNa solid catalyst shows increased HER (H_2 evolution rate) compared with pristine CNn sample. As listed in Table 1, the HER for the CNn is 55 μmol h^{-1}, while it is 303 μmol h^{-1} for CNa. It is tempting to conclude that the expanded surface area, optimized two-dimension piece structure and conjugated heterocyclic structure provides more exposed surface sites for electronic assemble. However, as reported previously, urea-derived g-C_3N_4 with the approximate specific surface area of CNa, only evolved H_2 at about 80 μmol h^{-1} [43]. Therefore, the activity enhancement was not mainly directly attributed to either surface area, but the degree of polymerization much determines H_2 evolution rates from water.

Fig. 9 shows the rate of H_2 evolution of CNa sample carried out under 4 h continuous visible light irradiation. Obviously, the amount of the produced H_2 linearly increases with the duration of visible light irradiation. This is an indication that the catalyst has robust stability for catalyzing H_2 generation as a function of irradiation time. Recycling stability for the catalyst is crucial basis in practical application. So the cycling H_2 evolution experiments were performed. The H_2 evolution rate was not decreased in every reaction cycle and after four consecutive runs (16 h), a total of 4.1 mmol

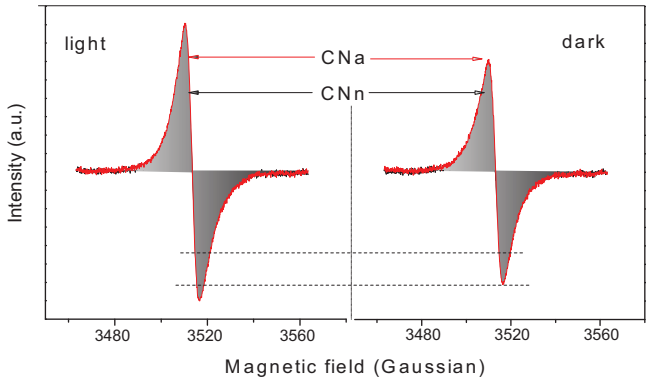

Fig. 8. UV–vis Solid-state EPR spectra of CNa and CNn with visible light (λ > 420 nm) or in the dark.

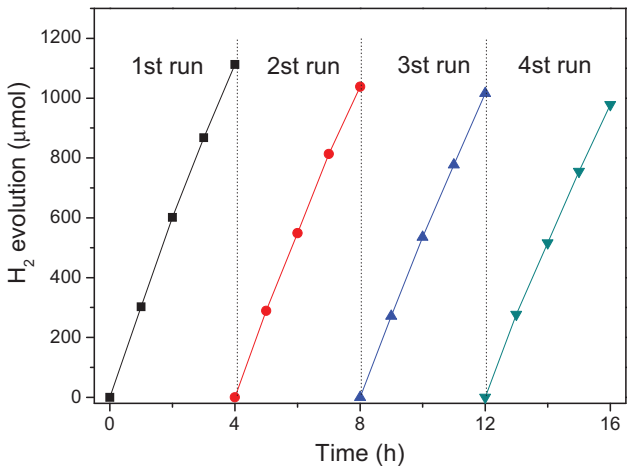

Fig. 9. Time course of H_2 evolution for CNa under visible light irradiation ($\lambda > 420$ nm).

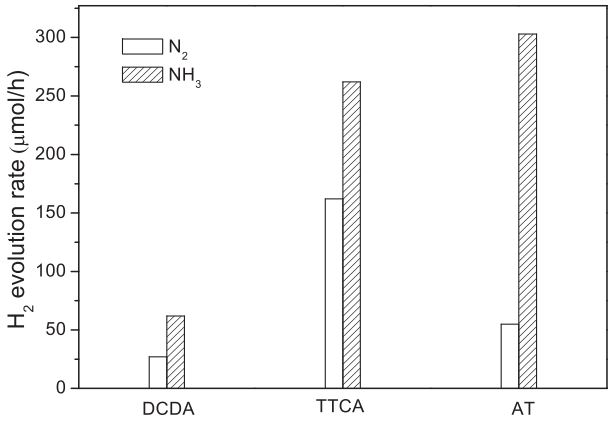

Fig. 10. photocatalytic activity of CNa and CNn prepared from different precursors for hydrogen evolution with visible light. (DCDA: dicyandiamide, TTCA: trithiocyanuric acid, AT: NH_4SCN).

H_2 gas (91.8 mL) is produced, and no obvious deactivation of the photocatalysts is found, suggesting the good stability of CNa as an polymer photocatalyst for solar H_2 generation.

Up to now, so many precursors including various organic/inorganic molecules have been recorded for the synthesis of g-C_3N_4 catalysts [43]. Whether this ammonia-polymerization route is applicable for other materials to prepare C_3N_4 with enhanced photocatalytic activity? To further confirm the versatility of this method, several typical precursor (dicyandiamide (DCDA), and trithiocyanuric acid (TTCA)) for C_3N_4 synthesis were selected and calcinated under identical ammonia conditions. The Photocatalytic activity for H_2 evolution is shown in Fig. 10. In addition of NH_4SCN, the obtained CNa samples prepared from DCDA and TTCA also possess higher photocatalytic activity than the corresponding CNn sample. Therefore, to synthesize low-defected C_3N_4 catalysts with enhanced photocatalytic activity for H_2 evolution from ammonia-polymerization could be achieved under so many conditions.

4. Conclusion

In summary, much condensed and low-defected C_3N_4 catalyst has been successfully synthesized from ammonia-polymerization method. The ammonia atmosphere during the calcination process decelerates the processing of the C_3N_4 condensation, offering an extra structure control for the synthesis of graphitic carbon nitride networks. Compared to the pristine C_3N_4 synthesized under nitrogen-polymerization method, the texture of the new catalyst was optimized to have higher surface area and smaller particles. In addition, lower defects and more intact sp^2 hybrid heptazine conjugate structure of C_3N_4 was realized. The large surface area, low-defected structure and enlarged band gap are supposed to be primary responsible for the enhanced photocatalytic activity of CNa. This work demonstrates a convenient route to synthesize low-defected C_3N_4 catalyst performed attractive photocatalytic activity without complex modification. It also provides enlightening information to design and synthesize novel polymer semiconductor photocatalysts with ordered crystallinity.

Acknowledgments

This work is financially supported by the natural science foundation of Jiangsu Province (Grant No. BK20140507).

References

[1] A. Mills, R.H. Davies, D. Worsley, Chem. Soc. Rev. 22 (1993) 417–425.
[2] H. Kisch, Angew. Chem. Int. Ed. 52 (2013) 812–847.
[3] A. Mishra, P. Bäuerle, Angew. Chem. Int. Ed. 51 (2012) 2020–2068.
[4] Y. Inoue, Energy Environ. Sci. 2 (2009) 364–386.
[5] J.H. Yang, H.J. Yan, X.L. Wang, F.Y. Wen, Z.J. Wang, D.Y. Fan, J.Y. Shi, C. Li, J. Catal. 290 (2012) 151–157.
[6] X.C. Wang, K. Maeda, A. Thomas, K. Takanabe, G. Xin, J.M. Carlsson, K. Domen, M. Antonietti, Nat. Mater. 8 (2008) 76–82.
[7] Y. Zheng, J. Liu, J. Liang, M. Jaroniecc, S.Z. Qiao, Energy Environ. Sci. 5 (2012) 6717–6731.
[8] K. Schwinghammer, M. Mesch, V. Duppel, C. Ziegler, J. Senker, B. Lotsch, J. Am. Chem. Soc. 136 (2014) 1730–1733.
[9] J. Liu, Y. Liu, N.Y. Liu, Y.Z. Han, X. Zhang, H. Huang, Y. Lifshitz, S.-T. Lee, J. Zhong, Z.H. Kang, Science 347 (2015) 970–974.
[10] J.H. Sun, J.S. Zhang, M.W. Zhang, M. Antonietti, X.Z. Fu, X.C. Wang, Nat. Commun. 3 (2012) 1139–1145.
[11] J.H. Huang, M. Antonietti, J. Liu, J. Mater. Chem. A. 2 (2014) 7686–7693.
[12] G.H. Dong, K. Zhao, L.Z. Zhang, Chem. Commun. 48 (2012) 6178–6180.
[13] T.Y. Ma, J.R. Ran, S. Dai, M. Jaroniec, S.Z. Qiao, Angew. Chem. Int. Ed. 54 (2015) 4646–4650.
[14] Z.Z. Lin, X.C. Wang, ChemSusChem 7 (2014) 1547–1550.
[15] S. Obregón, G. Colón, Appl. Catal. B Environ. 144 (2014) 775–782.
[16] L. Ge, F. Zuo, J. k. Liu, Q. Ma, C. Wang, D.Z. Sun, L. Bartels, P.Y. Feng, J. Phys. Chem. C 116 (2012) 13708–13714.
[17] Y. Zheng, L.H. Lin, X.J. Ye, F.S. Guo, X.C. Wang, Angew. Chem. Int. Ed. 53 (2014) 11926–11930.
[18] J. Liu, J.H. Huang, D. Dontosova, M. Antonietti, RSC Adv. 3 (2013) 22988–22993.
[19] Y. Ishida, L. Chabanne, M. Antonietti, M. Shalom, Langmuir 30 (2014) 447–451.
[20] W. Ho, Z.Z. Zhang, W. Lin, S. Huang, X.W. Zhang, X.X. Wang, Y. Huang, ACS Appl. Mater. Interfaces 7 (2015) 5497–5505.
[21] Q. Su, J. Sun, J.Q. Wang, Z.F. Yang, W.G. Cheng, S.J. Zhang, Catal. Sci. Technol. 4 (2014) 1556–1562.
[22] Q.Y. Lin, L. Li, S.J. Liang, M.H. Liu, J.H. Bi, L. Wu, Appl. Catal. B Environ. 163 (2015) 135–142.
[23] P. Niu, G. Liu, H.M. Cheng, J. Phys. Chem. C 116 (2012) 11013–11018.
[24] P. Niu, L.-C. Yin, Y.-Q. Yang, G. Liu, H.-M. Cheng, Adv. Mater. 26 (2014) 8046–8052.
[25] R. Noriega, J. Rivnay, K. Vandewal, F.P.V. Koch, N. Stingelin, P. Smith, M.F. Toney, A. Salleo, Nat. Mater. 12 (2013) 1038–1044.
[26] M. Shalom, S. Inal, C. Fettkenhauer, D. Neher, M. Antonietti, J. Am. Chem. Soc. 135 (2013) 7118–7121.
[27] Y.B. Li, H.M. Zhang, P.R. Liu, D. Wang, Y. Li, H.J. Zhao, Small. 9 (2013) 3336–3344.
[28] J.D. Hong, Y.S. Wang, Y.B. Wang, W. Zhang, R. Xu, ChemSusChem 6 (2013) 2263–2268.
[29] F. He, G. Chen, Y.G. Yu, Y.S. Zhou, Y. Zheng, S. Hao, Chem. Commun. 51 (2015) 6824–6827.
[30] H.Y. Zhang, A.C. Yu, J. Phys. Chem. C 118 (2014) 11628–11635.
[31] X.-H. Li, J.S. Zhang, X.F. Chen, A. Fischer, A. Thomas, M. Antonietti, X.C. Wang, Chem. Mater. 23 (2011) 4344–4348.
[32] T. Sano, S. Tsutsui, K. Koike, T. Hirakawa, Y. Teramoto, N. Negishi, K. Takeuchi, J. Mater. Chem. A 1 (2013) 6489–6496.
[33] Y.J. Cui, J.S. Zhang, G.G. Zhang, J.H. Huang, P. Liu, M. Antonietti, X.C. Wang, J. Mater. Chem. 21 (2011) 13032–13039.
[34] A. Thomas, A. Fischer, F. Goettmann, M. Antonietti, J.O. Müller, R. Schlögl, J.M. Carlsson, J. Mater. Chem. 18 (2008) 4893–4908.
[35] M. Shalom, M. Guttentag, C. Fettkenhauer, S. Inal, D. Neher, A. Llobet, M. Antonietti, Chem. Mater. 26 (2014) 5812–5818.

[36] J.S. Zhang, M.W. Zhang, G.G. Zhang, X.C. Wang, ACS Catal. 2 (2012) 940–948.
[37] W.W. Lei, D. Portehault, R. Dimova, M. Antonietti, J. Am. Chem. Soc. 133 (2011) 7121–7127.
[38] (a) P. Niu, L.-C. Yin, Y.-Q. Yang, G. Liu, H.-M. Cheng, Adv. Mater. 26 (2014) 8046–8052;
(b) X.F. Chen, Y.S. Jun, K. Takanabe, K. Maeda, K. Domen, X.Z. Fu, X.C. Wang, M. Antonietti, Chem. Mater. 21 (2009) 4093–4095.
[39] K. Maeda, R. Kuriki, M.W. Zhang, X.C. Wang, O. Ishitani, J. Mater. Chem. A 2 (2014) 15146–15151.
[40] H.Y. Zhang, A.C. Yu, J. Phys. Chem. C 118 (2014) 11628–11635.
[41] J. Liu, J.H. Huang, H. Zhou, M. Antonietti, ACS Appl. Mater. Interfaces 6 (2014) 8434–8440.
[42] J.S. Zhang, G.G. Zhang, X.F. Chen, S. Lin, L. Möhlmann, G. Dołega, G. Lipner, M. Antonietti, S. Blechert, X.C. Wang, Angew. Chem. Int. Ed. 124 (2012) 3183–3187.
[43] G.G. Zhang, J.S. Zhang, M.W. Zhang, X.C. Wang, J. Mater. Chem. 22 (2012) 8083–8091.